Received: 4 October 2017 | Revised: 15 December 2017 | Accepted: 28 December 2017 | Published on: 2 March 2018

DOI: 10.1002/ctpp.201700137

ORIGINAL ARTICLE

Contributions to Plasma Physics

Continuum kinetic modelling of cross-separatrix plasma transport in a tokamak edge including self-consistent electric fields

Mikhail Dorf | **Milo Dorr**

Lawrence Livermore National Laboratory, Livermore, California, USA

***Correspondence**
Mikhail Dorf, Lawrence Livermore National Laboratory, Livermore, California, USA.
Email: dorf1@llnl.gov

Funding Information
This research was supported by the U.S. Department of Energy, DE-AC52-07NA27344.

Eulerian kinetic calculations are presented for the axisymmetric cross-separatrix plasma transport at the edge of a tokamak. The simulations are performed with a high-order finite volume code COGENT, which solves the long-wavelength limit of the full-f ion gyrokinetic equation including the non-linear Fokker–Plank collision model. Self-consistent 2D electrostatic potential variations are obtained from the quasi-neutrality ($\boldsymbol{\nabla}\cdot\mathbf{j}=0$) equation coupled to an isothermal fluid electron response. Illustrative solutions presented for parameters characteristic of the DIII-D tokamak show qualitative agreement with experimental data.

KEYWORDS
finite-volume methods, gyrokinetics, tokamak edge

1 | INTRODUCTION

Kinetic effects play a significant role in defining tokamak plasma transport as the collisional mean free path in hot fusion-grade plasmas becomes large compared to the length scale for density and temperature variations along the magnetic field lines. While numerical modelling of magnetized plasma kinetics is a challenging problem, substantial simplification occurs in a tokamak core region, where the plasma species distribution is close to Maxwellian. As such, kinetic (i.e., gyrokinetic) core codes are typically employed to model small delta-F deviations from a Maxwellian distribution, which generate neoclassical (collisional)[1,2] and turbulent[3,4] fluxes. These fluxes can then be passed to low-dimensionality fluid transport codes to update the background plasma profiles. However, the presence of a steep gradient region in the edge of a tokamak, for example, under H-mode conditions, can lead to pronounced deviations of a background ion distribution function from a local Maxwellian. Therefore, gyrokinetic edge codes should include modelling of the background quasi-equilibrium dynamics, that is, a full-F approach is required.

Motivated in part by the success of continuum (Eulerian) delta-F codes for core physics and in part by their potential for high accuracy, the Edge Simulation Laboratory collaboration[5] has been developing a full-F code called COGENT for the edge.[6–8] The code is based on a high-order mapped multi-block finite-volume discretization scheme that involves the use of multiple grid blocks to represent complex magnetic topologies, including a divertor geometry.[9–11] In this paper, we focus on the 4D version of the code, which describes axisymmetric transport properties of edge plasmas. The present 4D model considers large-scale ($\rho_i/L_\perp << 1$) electrostatic potential variations corresponding to a quasi-equilibrium background, and solves full-F gyrokinetic equations for plasma species in the long-wavelength (drift-kinetic) limit. Here, ρ_i is the ion thermal gyroradius and $L_\perp$ is the characteristic length scale for perpendicular variations. The full non-linear Fokker–Plank collision operator[12] is used to describe ion–ion Coulomb collisions, and an ad hoc model is available to include the effects of anomalous (turbulent) transport.[13] Previous cross-separatrix COGENT simulations[7] used either prescribed, that is, non-evolving, potential variations, or a simplified 1D flux-surface average model for E_r involving ad hoc extrapolation into the open field line region. Here, we extend the simulation model to include 2D self-consistent variations of electrostatic potential on both open and closed field lines.

Determining the model for self-consistent quasi-equilibrium electric fields in a tokamak edge is an important and challenging problem. In contrast to the core region where the plasma profiles are nearly uniform on magnetic flux surfaces, and thereby the poloidal variations of a background electrostatic potential are weak, $\phi_{core}(\psi,\theta)\approx\phi_{core}(\psi)$, the edge plasma profiles can exhibit strong poloidal variations, and therefore $\phi_{edge}(\psi,\theta)$ can have a pronounced 2D structure. Also, the physical mechanisms that

set the radial electric field on open and closed field lines are different, which can lead to the development of narrow transition structures around the magnetic separatrix. In more detail, "neoclassical ion physics" sets radially confining E_r on closed field lines,[14,15] whereas "parallel electron physics", subject to the sheath boundary conditions at divertor plates, sets the electric fields on open field lines.[16–18] Nevertheless, it should also be mentioned that the presence of non-intrinsically-ambipolar processes in edge plasmas such as prompt orbit losses and charge-exchange collisions with neutrals can justify the use of the standard low-order gyrokinetic models for determining the quasi-equilibrium E_r.[19] This is in contrast to the core region, where the intrinsic ambipolarity of electron and ion transport may require the use of higher order gyrokinetic formulations[20] going beyond the standard numerical implementations.

In this paper, we propose a 2D model for self-consistent axisymmetric variations of the electrostatic potential based on the quasi-neutrality condition $\boldsymbol{\nabla}\cdot\boldsymbol{j}=0$, where $\boldsymbol{j}$ is the electrical current density summed over all plasma species. Evidently, the most accurate description of the plasma current carried by particle gyrocenters can be obtained by solving the gyrokinetic equations for the electron and ion species. However, the presence of fast parallel electron streaming, $\omega_{tr,e} \sim V_{T_e}k_\parallel$, and the even more rapid electrostatic Alfven mode[21] $\omega_H \sim \Omega_i\sqrt{m_i/m_e}(k_\parallel/k_\perp) = V_{T_e}k_\parallel/(k_\perp\rho_s)$ imposes a severe constraint on the time step needed for the stability of explicit time integration schemes, thereby demanding significant computational resources. Here, V_{T_e} is the electron thermal velocity, Ω_i is the ion cyclotron frequency, $\rho_s = \sqrt{m_e/m_i}V_{T_e}/\Omega_i$ is the ion-sound gyroradius, m_e and m_i are the electron and ion species mass, and $k_\parallel$ and $k_\perp$ are the parallel and perpendicular wave numbers. On the other hand, $\boldsymbol{\nabla}\cdot\boldsymbol{j}=0$ formulation offers a straightforward way to derive a reduced model that retains only ion kinetic effects and makes use of a fluid description for electrons. In particular, such a model can eliminate fast parallel electron dynamics associated with the electron inertia terms. Furthermore, the rapid processes corresponding to high parallel electron conductivity and heat diffusivity can be treated implicitly within a 2D fluid model framework, which is much less computationally intensive than implicit time integration of the original system that includes a 4D gyrokinetic equation for electrons.

It should be noted that electron kinetic effects can be important in the edge of a tokamak.[22–24] Indeed, even a cold and dense divertor plasma can be weakly collisional for the suprathermal tail particles, which contribute disproportionally to the parallel heat conductivity.[22] These kinetic effects can play a role in determining the electron temperature at the divertor plates, which in turn contributes to the scrape-off layer (SOL) radial electric field via the sheath boundary condition.[23] Nevertheless, the reduced kinetic-ion/fluid-electron hybrid model developed here captures the ion kinetic effects corresponding to ion orbit losses and poloidal variations of the ion distribution function, which play an important role in determining the self-consistent electric fields in the upstream SOL and inside the separatrix.

2 | SIMULATION MODEL

The 4D version of the COGENT code models the long-wavelength (i.e., drift-kinetic) limit of an axisymmetric gyrokinetic equation for a gyrocenter distribution function $f_\alpha(\mathbf{R}, v_\parallel, \mu, t)$ written in conservative form

$$\frac{\partial(B_{\parallel\alpha}^* f_\alpha)}{\partial t} + \boldsymbol{\nabla}\cdot(\dot{\mathbf{R}}_\alpha B_{\parallel\alpha}^* f_\alpha) + \frac{\partial}{\partial v_\parallel}(\dot{v}_{\parallel\alpha}B_{\parallel\alpha}^* f_\alpha) = C_\alpha[B_{\parallel\alpha}^* f_\alpha] + T_\alpha^{AN}[B_{\parallel\alpha}^* f_\alpha]. \tag{1}$$

Here, α denotes the particle species, $\boldsymbol{\nabla}$ is the gradient with respect to $\mathbf{R}$, and the guiding center velocity $\dot{\mathbf{R}}_\alpha$ is given by

$$\dot{\mathbf{R}}_\alpha = \frac{1}{B_{\parallel\alpha}^*}\left[v_\parallel \mathbf{B}_\alpha^* + \frac{1}{Z_\alpha e}\mathbf{b}\times(Z_\alpha e\boldsymbol{\nabla}\Phi + \mu\boldsymbol{\nabla}B)\right]. \tag{2}$$

The evolution of the guiding center parallel velocity is determined from

$$\dot{v}_{\parallel\alpha} = -\frac{1}{m_\alpha B_{\parallel\alpha}^*}\mathbf{B}_\alpha^*\cdot(Z_\alpha e\boldsymbol{\nabla}\Phi + \mu\boldsymbol{\nabla}B), \tag{3}$$

where m_α and Z_α are the species mass and charge state, respectively, e is the electron charge, $\Phi(\mathbf{R}, t)$ describes the long wavelength, $\rho_i/L_\perp << 1$, axisymmetric electrostatic potential variation, $\mathbf{B} = B\cdot\mathbf{b}$ is the magnetic field with $\mathbf{b}$ denoting the unit vector along the field, $\mathbf{B}_\alpha^*(\mathbf{R}, v_\parallel) \equiv \mathbf{B} + (m_\alpha/Z_\alpha e)v_\parallel\boldsymbol{\nabla}\times\mathbf{b}$, and $B_{\parallel\alpha}^* = \mathbf{B}_\alpha^*\cdot\mathbf{b}$. Finally, C_α and T_α^{AN} denote the collision and anomalous transport operators, for which a number of increasingly detailed options are available in COGENT.[12,13,25]

Equation 1 describes the full-F gyrokinetic equation that needs to be coupled to a model for self-consistent variations of an electrostatic potential. We begin the analysis by considering the long-wavelength limit of the gyro-Possion equation, which is often used in axisymmetric gyrokineic simulations[6,26–28]:

$$\sum_i \boldsymbol{\nabla}_\perp\cdot\left(\frac{Z_i^2 e^2 n_i}{m_i\Omega_i^2}\boldsymbol{\nabla}_\perp\Phi\right) = e\left(n_e - \sum_i Z_i\bar{n}_i\right). \tag{4}$$

TABLE 1 Characteristic near-separatrix parameters of a DIII-D H-mode

n_e (m^{-3})	T_i (eV)	T_e (eV)	B_ϕ (T)	Safety factor, q	R_0 (m)	m_i/m_p
10^{19}	300	50	1.6	3	1.6	2

Here, the sum is taken over the ion species, $\boldsymbol{\nabla}_\perp \equiv \boldsymbol{\nabla} - \mathbf{b}(\mathbf{b}\cdot\boldsymbol{\nabla})$ is the perpendicular gradient operator, $\Omega_i = Z_i eB/(m_i c)$ is the ion cyclotron frequency, $n_\alpha = (2\pi/m_\alpha)\int f_\alpha B^*_{\|\alpha} dv_\| d\mu$ is the ion species gyrocenter density, and $\overline{n}_i = (2\pi/m_i)\int [f_i + (m_i c^2/BZ_i^2 e^2)\mu\Delta_\perp^2 f_i] B^*_{\|i} dv_\| d\mu$ is the ion species gyro-averaged gyrocenter density, which is slightly different from n_i by the small "pressure-term" corrections. Taking the time derivatives of Equation 4 and making use of Equation 1, it follows

$$\sum_i \boldsymbol{\nabla}_\perp \cdot \left(\frac{Z_i^2 e^2 n_i}{m_i \Omega_i^2} \boldsymbol{\nabla}_\perp \frac{\partial \Phi}{\partial t} \right) = \boldsymbol{\nabla} \cdot \mathbf{j}_e + \boldsymbol{\nabla} \cdot \sum_i \mathbf{j}_i, \tag{5}$$

where in the left-hand side (LHS) of Equation (5) we neglected small time derivatives of the background ion density, which varies on a transport timescale $\tau_{transp} \sim L_\perp^2/D_A$ while retaining more rapid variations of the electrostatic potential, such as geodesic acoustic modes (GAMs), that occur on the transient timescale, $\tau_{tr} \sim a/V_{T_i}$. Here, D_A is the anomalous diffusivity, a is the tokamak minor radius, and V_{T_i} is the main ion species' thermal velocity. Neglecting the small "pressure-term" correction and assuming intrinsically ambipolar anomalous transport, the species gyrocenter current density that needs to be retained in the right-hand side (RHS) of Equation (5) is given by $\mathbf{j}_\alpha = Z_\alpha e \int \dot{\mathbf{R}}_\alpha f_\alpha B^*_{\|\alpha} dv_\| d\mu$. Equation (5) represents the plasma quasi-neutrality condition given by $\boldsymbol{\nabla}\cdot\mathbf{J} = 0$, where $\mathbf{J}$ is the total plasma current density, which includes the ion species' polarization current density $\mathbf{J}_p$, and the combined electron and ion gyrocenter current density $\mathbf{J}_{gc}$.

As mentioned earlier (Section 1), the gyrokinetic system in Equations (1) and (5) contains fast timescales related to the electron inertia, which introduces significant computational challenges. It is therefore of particular practical importance to develop a reduced model requiring less computational resources. Here, we propose the kinetic-ion/fluid-electron hybrid model, in which we treat electrons within a collisional fluid framework. It is worth noting that in the near-separatrix region the electron temperature can be substantially lower than the ion temperature, and therefore such a model can be justified. Indeed, considering, for example, an H-mode of the DIII-D tokamak[16,29] with the characteristic near-separatrix parameters shown in Table 1, we obtain $qR_0/(V_{T_i}\tau_i) \approx 0.03$ and $qR_0/(V_{T_e}\tau_e) \approx 1.2$, where τ_e and τ_i are the basic electron and ion collisional times given by Braginskii,[30] q is the magnetic safety factor, and R_0 is the tokamak major radius. We, however, emphasize again that an electron fluid model may fail to adequately describe suprathermal tail particles, which strongly contribute to the electron heat conductivity, and thereby affect the electron temperature and electrostatic potential near the divertor plates.

Considering, for simplicity, the case of a single ion species with $Z_i = 1$, and neglecting the small electron inertia, the parallel momentum equation for electrons yields

$$J_\| = \sigma_\| \left(\frac{1}{en_e} \nabla_\| P_e - \nabla_\| \Phi + \frac{0.71}{e} \nabla_\| T_e \right), \tag{6}$$

where $\sigma_\| = 1.96 n_e e^2 \tau_e/m_e$ is the parallel electron conductivity[30], $P_e = n_e T_e$ is the electron pressure, and T_e is the electron temperature. The parallel current density in Equation (6) is the total plasma current summed over the electron and ion species, $J_\| = J_{i,\|} + J_{e,\|}$. We note that the ion species' parallel current density $J_{i,\|}$ is slightly different from the corresponding ion gyrocenter current density $j_{i,\|}$ in Equation (5). In particular, the difference contains the term $en_{i,pol}V_{i,\|}$, where the ion polarization charge density $en_{i,pol}$ corresponds to the LHS of Equation (4), $V_{i,\|} = \mathbf{b}\cdot\mathbf{V}_i$, and $\mathbf{V}_i$ is the ion flow velocity. The contribution from this term, if retained in Equation (5), would include the term $(V_{i,\|}\cdot\nabla_\|)en_{i,pol}$, which corresponds to the parallel-convection piece of the ion polarization current, $\mathbf{J}_p = (c^2 m_i/Z_i eB^2)[\partial\boldsymbol{\nabla}_\perp\Phi/\partial t + (\mathbf{V}_i\cdot\boldsymbol{\nabla})\boldsymbol{\nabla}_\perp\Phi]$, and explicitly appears in the fluid framework.[31] Here, we neglect the small difference between the parallel plasma current and its gyrocenter counterpart and combine Equations (5) and (6) to obtain

$$\boldsymbol{\nabla}_\perp \cdot \left(\frac{e^2 n_i}{m_i \Omega_i^2} \boldsymbol{\nabla}_\perp \frac{\partial \Phi}{\partial t} \right) = \boldsymbol{\nabla}_\perp \cdot \mathbf{j}_{e,\perp} + \boldsymbol{\nabla}_\perp \cdot \mathbf{j}_{i,\perp} + \nabla_\| \left[\sigma_\| \left(\frac{1}{en_e} \nabla_\| P_e - \nabla_\| \Phi + \frac{0.71}{e} \nabla_\| T_e \right) \right]. \tag{7}$$

It is instructive to note that, because of the large value of the electron conductivity, the term $\nabla_\| J_\|$ dominates the RHS of Equation (7):

$$\frac{\boldsymbol{\nabla}_\perp \cdot (\mathbf{j}_{e,\perp} + \mathbf{j}_{i,\perp})}{\nabla_\| J_\|} \sim \frac{(\rho_i/R_0)(enV_{T_i}/L_P)}{(\sigma_\|/en)(\rho_\theta/L_T)nT_e(qR_0)^{-2}} \sim q\frac{V_{T_i}}{V_{T_e}}\frac{L_T}{L_P}\frac{B_\theta}{B}\frac{qR_0}{V_{T_e}\tau_e} \ll 1. \tag{8}$$

Here, $n = n_e \approx n_i$ denotes the plasma density, $\rho_\theta = (B_\theta/B)\rho_i$ is the poloidal ion gyroradius, L_T and L_P are the length scales for radial variations of the plasma temperature and pressure, respectively, $T_e \lesssim T_i$ and $\nabla_\| \sim (B_\theta/B)a^{-1}\partial/\partial\theta \sim 1/(qR_0)$ is assumed, and to estimate the parallel variations of plasma profiles (e.g., density) we made use of $\nabla_\|\tilde{f} \sim (\rho_i/R_0)F_M/L_T$, where $\tilde{f}$ denotes the

deviation of the ion distribution function from a Maxwellian background F_M with poloidally uniform density and temperature profiles. We note that the inequality in Equation (8) is formally not valid in close proximity to the X-point where $\nabla_\parallel \to 0$; however, that region is small and should not affect the global solution.

Making use of Equations (7) and (8), it follows that on a timescale larger than the fast electron time scale, $t \gg \tau_{cond} \sim (\rho_s/L_p)^2 \tau_e (qR_0/V_{T_e}\tau_e)^2$, a solution for the electrostatic potential has the form

$$\Phi(\psi,\theta,t) \approx C(\Psi,t) + \int d\theta \left(\frac{1}{en_e}\frac{\partial P_e}{\partial \theta} + \frac{0.71}{e}\frac{\partial T_e}{\partial \theta} \right), \tag{9}$$

where Ψ and θ are the magnetic flux function and the poloidal angle coordinate, respectively, and $C(\Psi, t)$ is the constant of integration. On open field lines, the function $C(\Psi, t)$ is determined by the sheath boundary conditions at the divertor plates (see, e.g., Refs. 32, 33). On closed field lines, it can be determined by taking the flux-surface average, $\langle Y \rangle(\psi) = \oint (\mathbf{B}\cdot\nabla\theta)^{-1} Y(\psi,\theta) d\theta / \oint (\mathbf{B}\cdot\nabla\theta)^{-1} d\theta$, of Equation (7). Note that on closed field lines $\langle \nabla_\parallel j_\parallel \rangle = 0$, and therefore the function $C(\psi, t) = \langle \Phi \rangle$, which determines the radial electric field, is set by the flux-surface average of the perpendicular plasma current $\langle \mathbf{j}_\perp \rangle$. Neglecting a small electron contribution to the flux-surface averaged current, $\langle \mathbf{j}_\perp \rangle \approx \langle \mathbf{j}_{i,\perp} \rangle$, and a small ion polarization density, $n_i \approx n_e$, we adopt the following equation to describe the evolution of self-consistent potential perturbations

$$\boldsymbol{\nabla}_\perp \cdot \left(\frac{e^2 n_i}{m_i \Omega_i^2} \boldsymbol{\nabla}_\perp \frac{\partial \Phi}{\partial t} \right) = \boldsymbol{\nabla}_\perp \cdot \mathbf{j}_{i,\perp} + \nabla_\parallel \left[\sigma_\parallel \left(\frac{1}{en_i} \nabla_\parallel P_e - \nabla_\parallel \Phi + \frac{0.71}{e} \nabla_\parallel T_e \right) \right], \tag{10}$$

where the ion perpendicular current is determined by

$$\mathbf{j}_{i,\perp} = \int \dot{\mathbf{R}}_{i,\perp} f_i B^*_{\parallel i} dv_\parallel d\mu, \tag{11}$$

and $\dot{\mathbf{R}}_{i,\perp} = \dot{\mathbf{R}}_i - (\dot{\mathbf{R}}_i \cdot \mathbf{b})\mathbf{b}$. We note that the term $\mathbf{j}_{e,\perp}$ neglected in Equation (10) can represent a pronounced contribution to a local value of the total perpendicular plasma current $\mathbf{j}_\perp$. Nevetheless, Equation (10) still sufficiently accurately describes the dynamics of self-consistent potential variations. The local effects of $\mathbf{j}_{e,\perp}$ can be, in principle, retained by removing the contribution from the ExB drift in Equation (11) and by adding the term $-\boldsymbol{\nabla}_\perp \cdot [(2P_e + m_e n_e V_{e,||}^2)(\mathbf{R}_c \times \mathbf{B})/(R_c B)^2]$ in the RHS of Equation (10), as is done in fluid codes.[31,34] Here, $\mathbf{R}_c$ is the radius of curvature of the magnetic field lines, and $V_{e,\parallel}$ is the electron parallel flow velocity.

While poloidal variations of an electrostatic potential are set by the parallel electron force balance and vary smoothly across the separatrix, the physical mechanisms that set the radial electric field, that is, the function $C(\psi, t)$ in Equation (9), are quite different on open and closed field lines (see the discussion that follows Equation (9)). Therefore, one can expect a rapid change in the value of a radial electric field E_r that occurs within a narrow layer around the separatrix.[16,18,31,33,35] Making use of the fact that the perpendicular ion current has an $\mathbf{E}_\perp$-dependent contribution[36] $\sim \boldsymbol{\nabla}_\perp \cdot (\sigma_{NC}\mathbf{E}_\perp)$, where $\sigma_{NC} \sim c^2 n_i T_i \tau_i/(BR_0)^2$ is the ion neoclassical conductivity, the width of the transition layer $L^{sep}_{E,NC}$ can be estimated from[36] $\boldsymbol{\nabla}_\perp \cdot (\sigma_{NC}\mathbf{E}_\perp) \sim \nabla_\parallel(\sigma_\parallel E_\parallel)$. Assuming $E_\parallel \sim T_e/(eqR_0)$ and $E_\perp \sim T_i/(eL^{sep}_{E,NC})$, it follows that

$$L^{sep}_{E,NC} \sim q\rho_i (T_i/T_e)^{5/4} (m_e/m_i)^{1/4}. \tag{12}$$

Taking, for illustrative purposes, the near-separatrix DIII-D parameters in Table 1, we obtain $L^{sep}_{E,NC} \sim 3.5\rho_i$.

The neoclassical estimate (in Equation (12)) for the transition layer width $L^{sep}_{E,NC}$ yields steep gradients of a background radial electric field, which approach the validity limits of the gyrokinetic theory. It is also instructive to assess the influence of other physical mechanisms, such as anomalous transport and charge-exchange collisions with neutrals, on the width of the transition layer. The effects of anomalous transport are included in our gyrokinetic model (see Equation (1)) via the ad hoc anomalous transport operator $T_i^{AN}[B^*_{\parallel i} f_i] = \boldsymbol{\nabla}_\perp \cdot \widehat{\mathbf{T}}_A(v_{||}, \mu, \mathbf{R}) \cdot \boldsymbol{\nabla}_\perp (B^*_{\parallel i} f_i)$, where the functional form of the matrix $\widehat{\mathbf{T}}_A$ can be chosen to match the "fluid" anomalous transport coefficients,[13] such as particle diffusivity ($\widehat{\mathbf{D}}_A$), heat diffusivity ($\widehat{\chi}_A$), and viscosity ($\widehat{\boldsymbol{\eta}}_A$). The anomalous transport opertor generates the zero-order $O(\rho_i^0/L_\perp^0)$ parallel force $F^A_{||} = n_i^{-1} \boldsymbol{\nabla}_\perp \cdot \widehat{\boldsymbol{\eta}}_A \cdot \boldsymbol{\nabla}_\perp V_{i||}$, which plays an important role in setting the ion toroidal flow. However, the contribution of intrinsically ambipolar anomalous transport, $\int T_i^{AN}[B^*_{\parallel i} f_i] dv_\parallel d\mu = \int T_e^{AN}[B^*_{\parallel e} f_e] dv_\parallel d\mu$, to the total plasma current is rather small. It is generated by the first-order $O(\rho_i/L_\perp)$ perpendicular force,[33–35] $F^A_\perp = n_i^{-1} \boldsymbol{\nabla} \cdot \widehat{\boldsymbol{\eta}}_A \cdot \boldsymbol{\nabla} V_{i,\perp}$, which drives the second-order $O(\rho_i^2/L_\perp^2)$ perpendicular ion current $\mathbf{j}^A_{i,\perp} = n_i c B^{-1} [\mathbf{F}^A_\perp \times \mathbf{b}]$. Here, $\mathbf{V}_{i,\perp}$ is the first-order ion drift velocity, which includes the diamagnetic and E x B drifts. In the near-separatrix region, where the electrostatic potential exhibits strong radial variations, the anomalous transport contribution to the ion current is dominated by $j^A_{i,\perp} \sim c^2 B^{-2} \nabla_\perp \eta_{A,\perp} \Delta_\perp \Phi$, and the transition width $L^{sep}_{E,AN}$ can be estimated from $\nabla_{||}(\sigma_{||} E_{||}) \sim \boldsymbol{\nabla}_\perp \cdot \mathbf{j}^A_{i,\perp}$ to give

$$L^{sep}_{E,AN} \sim \rho_i \left(\frac{D_A}{\rho_i^2/\tau_i} \frac{qR_0}{V_{T_i}\tau_i} \frac{qR_0}{V_{T_e}\tau_e} \sqrt{\frac{T_i}{T_e}} \sqrt{\frac{m_e}{m_i}} \right)^{1/4}, \tag{13}$$

where $D_A = \eta_{A,\perp}/(m_i n_i)$ is the characteristic value of the anomalous transport coefficients. Considering the near-separatrix DIII-D H-mode parameters in Table 1 and assuming $D_A \sim 1$ [m^2/s], we obtain $L_{E,AN}^{sep} \sim 0.7\rho_i$.

It is instructive to compare the neoclassical and anomalous transport contributions to the ion current. On closed field lines, where the radial electric field is determined by the flux surface average of the perpendicular ion current, the neoclassical contribution is given by

$$\langle j_{i,r} \rangle \simeq \sigma_{NC}[E_r - E_{NC}(V_{i,||})], \tag{14}$$

where E_{NC} is the neoclassical quasi-equilibrium radial electric field, determined in the large aspect ratio limit by[14] $E_{NC} = (V_{i,\parallel}/c)B_\theta + (1/en_i)dP_i/dr - (k/e)dT_i/dr$, where k is the collisionality-dependent coefficient, with $k = 1.17$ in the weakly collisional regime and $k = -1.7$ in the strongly collisional regime. Estimating the anomalous contribution to the flux-surface averaged perpendicular current as $\langle j_{i,r}^A \rangle \sim c^2 \eta_{A,\perp} E_r/(L_\perp B)^2$, it follows that such a contribution should be retained provided $L_\perp \le \rho_i (R_0/V_{T_i}\tau_i)\sqrt{\tau_i D_A/\rho_i^2}$. For the DIII-D parameters used earlier, this estimate yields a very short length scale $L_\perp \le 0.14\rho_i$. Finally, we note that, although the effects of the anomalous transport associated with the perpendicular ("classical") forces might not play a strong role in defining the radial electric field, the parallel ("neoclassical") forces included in the operator $T_i^{AN}[B_{\parallel i}^* f_i]$ can strongly influence the ion parallel flow velocity,[7] and thereby the corresponding value of the neoclassical quasi-equilibrium radial electric field (see Equation (14)).

Similarly, we can evaluate the effects of charge-exchange collisions with neutrals. Assuming that the interaction with the neutrals is described by the force $\mathbf{F}^{cx} = -m_i \nu_{cx}(\mathbf{V}_i - \mathbf{V}_n)$, the second-order $O(\rho_i^2/L_\perp^2)$ contribution to the perpendicular ion current is given by $\mathbf{j}_{i,\perp}^{cx} = n_i c B^{-1}[\mathbf{F}_\perp^{cx} \times \mathbf{b}]$ and the corresponding width of the transition layer is

$$L_{E,cx}^{sep} \sim \rho_i \left(\nu_{cx}\tau_i \frac{qR_0}{V_{T_i}\tau_i} \frac{qR_0}{V_{T_e}\tau_e} \sqrt{\frac{T_i}{T_e}} \sqrt{\frac{m_e}{m_i}} \right)^{1/2}. \tag{15}$$

Here, $\mathbf{V}_n$ is the neutral flow velocity, $\nu_{cx} = (\sigma v)_{cx} n_n$ is the charge-exchange frequency, $(\sigma v)_{cx} \sim 3.2\times 10^{-15}\sqrt{T_i[\mathrm{eV}]/0.026}$ m^3/s is the charge-exchange reactivity,[31] and n_n is the neutral density. For the case of the DIII-D parameters (see Table 1), the transition width in Equation (15) becomes the order of the ion gyroradius $L_{E,cx}^{sep} \sim \rho_i$ for $n_n \sim 2\times 10^{18}$ m^{-3}. Note, however, that typical values of the neutral density in the DIII-D midplane separatrix region are much smaller. It is also straightforward to show that the ion current driven by the perpendicular charge-exchange forces is much less than its neoclassical counterpart, $j_{i,\perp}/j_{i,\perp}^{cx} \sim \nu_{cx} R^2/(V_{T_i}^2\tau_i) << 1$, for typical near-separatrix parameters. On the other hand, the parallel charge-exchange force may play a role in determining plasma toroidal rotation[19] (and thereby $V_{i,\parallel}$ in Equation (14)), especially in regimes where the anomalous transport is suppressed. Including the parallel charge-exchange effects into the COGENT simulation model will be a subject of our future studies. Finally, it is instructive to note that if the second-order $O(\rho_i^2/L_\perp^2)$ corrections $\mathbf{j}_{i,\perp}^A$ and/or $\mathbf{j}_{i,\perp}^{cx}$ are retained in Equation (7) (or Equation (10)), then it is still sufficient to use the first-order $O(\rho_i/L_\perp)$ gyrokinetic equation (1) to obtain the required fluid quantities (i.e., moments of f_i). In other words, it is not necessary to include the corresponding second-order drift velocities $\mathbf{V}_{i,\perp}^{A,cx} = \mathbf{j}_{i,\perp}^{A,cx}/(en_i)$ in Equation (1).

While the "perpendicular" effects of anomalous transport and charge-exchange collisions do not appear to play a pronounced role in determining electrostatic potential variations, we, nevertheless, extend Equation (10) to include the "perpendicular" charge-exchange term and assume artificially high values of the near-separatrix neutral density in order to provide smoothing of a numerical solution in the transition region. As a result, the quasi-neutrality equation for the electrostatic potential takes the form

$$\nabla_\perp \cdot \left(\frac{e^2 n_i}{m_i \Omega_i^2} \nabla_\perp \frac{\partial \Phi}{\partial t} \right) = \nabla_\perp \cdot \mathbf{j}_{i,\perp} + \nabla_\parallel \left[\sigma_\parallel \left(\frac{1}{en_i} \nabla_\parallel P_e - \nabla_\parallel \Phi + \frac{0.71}{e} \nabla_\parallel T_e \right) \right] - \nabla_\perp \cdot \left(\frac{c^2 m_i n_i \nu_{cx}}{B^2} \nabla_\perp \Phi \right). \tag{16}$$

Equation (16) along with Equations (1)–(3) represent the COGENT simulation model that needs to be coupled with a model for an electron temperature. For simplicity, here we assume isothermal electrons with $T_e = \mathrm{const}$, and $P_e = n_i T_e$. Development of a more detailed electron model model will be the subject of our future studies.

3 | COGENT IMPLEMENTATION

A detailed description of the COGENT numerical algorithms is given elsewhere.[10] In this section, we briefly summarize the main features of the code and certain aspects specific to the present application.

3.1 | Spatial discretization

The code utilizes a high-order finite-volume method[9] combined with mapped-multiblock technology,[11] in which the entire grid structure is represented by a union of grid blocks with a smooth function defined on each block to map the physical coordinate system onto a logically rectangular (computational) grid and with high-order interpolation methods used for intra-block communication. To exploit strong anisotropy of plasma transport, the grid is flux-aligned everywhere excluding a small vicinity of the X-point, where it is smoothly extended towards (and beyond) the block boundaries to enable high-order treatment of the X-point region. Note that fully flux-aligned grids, which are typically used in edge plasma modelling,[31,34] have diverging metric coefficients at the X-point (as evidenced by the kink in the poloidal magnetic field), thereby posing a problem for high-order methods.

Successful application of a fourth-order accurate numerical algorithm involving departure of a COGENT grid from the magnetic flux surfaces near the X-point was previously demonstrated in simulations with a fixed electrostatic potential distribution.[7,10] However, extending the physics model to include self-consistent potential variations (in Equation (16)) while maintaining the same grid structure led to significantly degraded spatial convergence properties. To elucidate that fact, we note the "anisotropic nature" of plasma transport becomes more pronounced (thus, less tolerable to grid-line departure from the flux surfaces) when the electron physics is included. More quantitative analysis can be done as follows. From Equation (16), it follows that an accurate numerical solution for a radial electric field E_r in the closed-field-line region requires a truncation error from the numerical evaluation of $\langle \nabla_\parallel J_\parallel \rangle$ (equal to zero in a continuum space) to be much smaller than $\langle \boldsymbol{\nabla}_\perp \cdot \mathbf{j}_{i,\perp} \rangle$. Neglecting, for simplicity, poloidal variations in plasma profiles, that is, $\Phi \approx \Phi(\psi)$ and $n_i \approx n_i(\psi)$, we can estimate the truncation error $Er\{\nabla_\parallel J_\parallel\}$ within the de-aligned region, $|\mathbf{R} - \mathbf{R}_x| < r_x$, as $Er\{\nabla_{||} J_{||}\} \sim \sigma_\parallel (B_{\theta,x}/B)^2 (T_i/eL_{p,x}^2)(\Delta_{x,e}/L_{p,x})^n$. Here, n is the order of accuracy, $\mathbf{R}_x$ is the X-point coordinate, r_x is the characteristic size of the de-aligned region, $B_{\theta,x}$, $L_{p,x}$, and $\Delta_{x,e}$ are the poloidal magnetic field, length scale for plasma profile variations, and the grid cell size within the de-aligned region, respectively, and we assumed $|\boldsymbol{\nabla}\Phi| \sim T_i/eL_{p,x}$. Estimating $B_{\theta,x} \sim (r_x/a)B_\theta$ and $L_{p,x} \sim (r_x/a)L_p$, where B_θ and L_p denote the poloidal magnetic field and the radial length scale for plasma profile variations at the outer midplane, the condition $Er\{\langle \nabla_\parallel J_\parallel \rangle\} \ll \langle \boldsymbol{\nabla}_\perp \cdot \mathbf{j}_{i,\perp} \rangle$ implies

$$\left(\frac{\Delta_{x,e}}{L_{p,x}}\right)^n \ll \left(\frac{\rho_i}{R_0}\right)^2 \left(\frac{B}{B_\theta}\right)^3 \left(\frac{T_e m_e}{T_i m_i}\right)^{1/2} \left(\frac{L_p}{V_{T_e}\tau_e}\right) \left(\frac{a}{r_x}\right)^5, \tag{17}$$

where we made use of $\langle \boldsymbol{\nabla}_\perp \cdot \mathbf{j}_{i,\perp} \rangle \sim (\rho_i/R_0)(\rho_\theta/L_p) e n_i V_{T_i}$ and estimated the contribution of the de-aligned region into a flux-surface average as a/r_x. Considering the near-separatrix DIII-D parameters in Table 1, and taking $B_\theta/B \sim 0.2$ and $L_p \sim 1$ cm for H-mode conditions, we obtain a strong constraint on the size of a cell $(\Delta_{x,e}/L_{p,x})^n \ll 4 \times 10^{-9} (a/r_x)^5$. It is instructive to note that accurate modelling of anisotropic ion dynamics (see Equation (1)) in the de-aligned region imposes a less severe limitation on the cell size $\Delta_{x,i}$ determined from $Er\{v_\parallel \nabla_\parallel F\} \ll \mathbf{v}_m \cdot \boldsymbol{\nabla}_\perp F$, where $|\mathbf{v}_m| \sim (\rho_i/R_0) V_{T_i}$ is the ion magnetic drift velocity. Estimating the truncation error in the de-aligned region as $Er\{v_{||} \nabla_{||} F\} \sim V_{T_i} (B_{\theta,x}/B) L_{p,x}^{-1} (\Delta_{x,i}/L_{p,x})^n \sim V_{T_i} (B_\theta/B) L_p^{-1} (r_x/a)^2 (\Delta_{x,i}/L_{p,x})^n$, we obtain

$$\left(\frac{\Delta_{x,i}}{L_{p,x}}\right)^n \ll \left(\frac{\rho_i}{R_0}\right) \left(\frac{B}{B_\theta}\right) \left(\frac{a}{r_x}\right). \tag{18}$$

For the DIII-D parameters, the inequality in Equation (18) takes the form $(\Delta_{x,i}/L_{p,x})^n \ll 7 \times 10^{-3} (a/r_x)^2$, and assuming $r_x \sim 0.2a$, as typically used in COGENT simulations, we obtain that $\Delta_{x,e} \sim 0.14 \Delta_{x,i}$.

While more detailed studies of fourth-order simulations including grid dealignment near the X-point and the self-consistent potential model in Equation (16) are under way, here we utilize the lower order flux-aligned version of the code. In this version, the grid shown in Figure 1a is fully aligned with magnetic flux surfaces, and a second-order discretization is used to solve Equation (16) for the electrostatic potential and to evaluate the gyrokinetic velocity in Equations (2) and (3). The numerical fluxes on cell faces in Equation (1) are then computed by making use of a third-order upwind scheme. It is important to note that by applying a finite-volume method to Equation (16) and postulating a zero contribution from $\nabla_\parallel J_\parallel$ to the radial fluxes (i.e., numerical fluxes normal to the radial cell faces), we enforce discrete annihilation of the term $\langle \nabla_\parallel J_\parallel \rangle$, and therefore remove the severe cell-size constraint in Equation (17). Details of the grid-generation algorithm will be reported in our future publications, while here we only mention that the mesh is locally orthogonal everywhere except near the block boundaries (see Figure 1a). Such construction avoids small poloidal cell size near the block boundaries observed for the case of a fully locally orthogonal grid.[31,34,35] For an explicit time integration scheme, the presence of small poloidal cells would significantly restrict a stable time step determined by the Courant constraint.

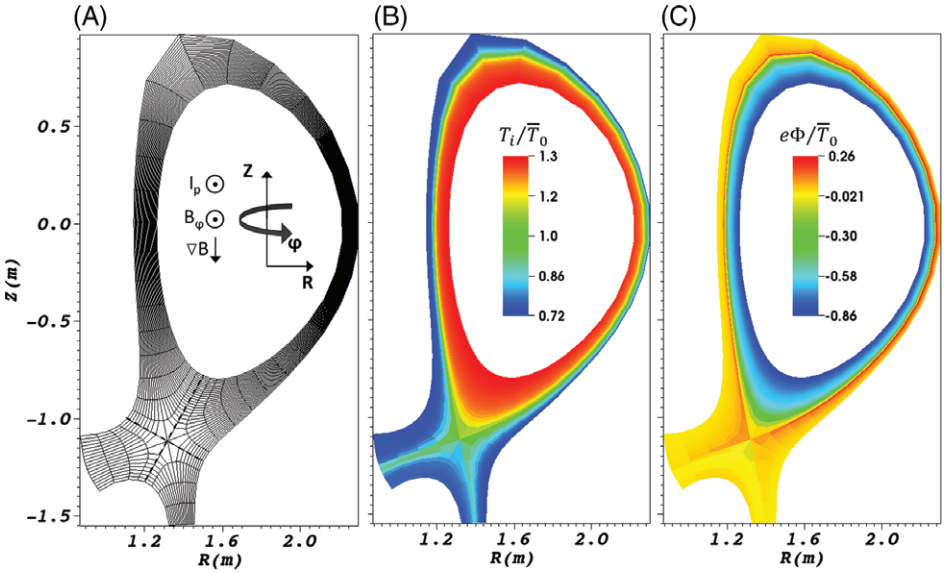

FIGURE 1 Results of the illustrative numerical simulations. Frame (a) shows the flux-aligned mesh used in the simulations. The mesh is locally orthogonal everywhere except near the cuts (illustrated by bold dashed lines), which correspond to the block boundaries. Frames (b) and (c) show the solutions for the ion temperature and electrostatic potential at $t = 2.8$ ms, respectively

3.2 | Zero-order errors from B-field data

As mentioned earlier (see Section 1), the COGENT code solves the full-F gyrokinetic equation (Equation (1)), which contains both zero-order $O(\rho_i^0/L_\perp^0)$ and first-order $O(\rho_i/L_\perp)$ terms. The zero-order terms in the LHS of Equation (1) include

$$GK_0[f_i(\mathbf{R}, v_{||}, \mu)] = \boldsymbol{\nabla} \cdot (v_{||}\mathbf{B}f_i) + \frac{\partial}{\partial v_{||}}\left(-\frac{\boldsymbol{\nabla}B \cdot \mathbf{B}}{2m_i}\mu f_i\right). \tag{19}$$

The operator $GK_0[f_i]$ annihilates a Maxwellian distribution function with poloidally uniform density $n = n(\psi)$ and temperature $T = T(\psi)$ profiles, $f_i = f_M = n(m_i/2\pi T)^{3/2}\exp(-m_i v_{||}^2/2T - \mu B/T)$, in a continuum space. However, a discrete evaluation of $GK_0[f_M]$ yields a zero-order $O(\rho_i^0/L_\perp^0)$ truncation error. An accurate numerical solution of the full-F problem (in Equation (1)) requires this zero-order numerical error to be much smaller than the first-order physical terms. Provided that all the quantities in Equation (19) are resolved by a phase-space grid, an ordered truncation error in evaluation of the LHS of Equation (1), which asymptotically decreases with the cell size as Δ^n, is guaranteed by a continuum numerical method of the nth order. For the case of an ideal magnetic geometry, the length scale for variations of the background magnetic field in Equation (19) is typically larger than that for the ion distribution function, $L_B^{id} > L_f$. However, experimental data for the magnetic field (often provided in the form of magnetic flux function) may contain a short-scale noise, $L_B^{noise} < L_f$. As a result, a pronounced zero-order $O(\rho_i^0/L_\perp^0)$ numerical error can be produced even if the grid resolves the distribution function variations, $\Delta < L_f$. To alleviate this issue, two methods are implemented in the COGENT code. The first method involves the application of a smoothing technique to the input magnetic field data in order to suppress high-frequency noise. In the second approach, a "flux-surface averaged" Maxwellian fit f_M^{fit} is subtracted from a solution f_i, and $GK_0[f_M^{fit}] = 0$ is discretely enforced. The density and temperature profiles of the Maxwellian fit, $n_{fit}(\psi)$ and $T_{fit}(\psi)$, are obtained as a flux-surface average of the ion density $n_i(\psi, \theta)$ and temperature $T_i(\psi, \theta)$ on closed field lines and as poloidal averages between the divertor plates on open field lines. Note that Equation (19) involves only the parallel-to-**B** derivatives, and therefore a discontinuity in the $n_{fit}(\psi)$ and $T_{fit}(\psi)$ quantities across the magnetic separatrix is not differentiated. Denoting the Vlasov operator in Equation (1) as $\boldsymbol{\nabla} \cdot (\dot{\mathbf{R}}_i B_{||_i}^* f_i) + \frac{\partial}{\partial v_{||}}(\dot{v}_{||_i} B_{||_i}^* f_i) \equiv GK[f_i] \equiv GK_0[f_i] + GK_1[f_i]$, we numerically evaluate it by making use of

$$GK[f_i] = GK_0[f_i - f_M^{fit}] + GK_1[f_i]. \tag{20}$$

This method improves numerical accuracy for the case where the ion distribution function is close to an unshifted Maxwellian distribution with poloidally uniform density and temperature profiles, which corresponds to a shallow-gradient region (e.g., top of a pedestal) with a drift-ordered plasma rotation velocity. Note that in the opposite limit, where the zero- and first-order terms in Equation (1) are comparable (e.g., mid-point of an H-mode pedestal), numerical errors generated by a small B-field noise are less important.

3.3 | Temporal discretization

For the parameters of the illustrative simulations presented in this work, the Courant time-step constraint is roughly similar for the Vlasov, collision, and anomalous transport terms in Equation (1), and therefore an explicit fourth-order Runge–Kutta

time integration scheme is used to advance the ion gyrokinetic equation. We note that implicit-explicit (IMEX) time integration methods, which enable implicit time integration of selected terms such as collisions and anomalous transport, are available in COGENT[37,38] as well. In contrast, Equation (16) for the electrostatic potential variations yields a fast electron timescale $\tau_{cond} \sim (\rho_s/L_p)^2\tau_e(qR_0/V_{T_e}\tau_e)^2 \gg R_0/V_{T_i}$ (see Section 2), and therefore requires implicit treatment. Here, we adopt a simple first-order backward-Euler scheme and advance Equation (16) in time as follows:

$$\boldsymbol{\nabla}_\perp \cdot \left(\frac{e^2 n_i}{m_i \Omega_i^2} \boldsymbol{\nabla}_\perp \frac{\Phi^{(l+1)} - \Phi^{(l)}}{\Delta_t} \right) = \boldsymbol{\nabla}_\perp \cdot \mathbf{j}_{i,\perp} + \nabla_\parallel \left[\sigma_\parallel \left(\frac{T_e}{e n_i} \nabla_\parallel n_i - \nabla_\parallel \Phi^{(l+1)} \right) \right] - \boldsymbol{\nabla}_\perp \cdot \left(\frac{c^2 m_i n_i \nu_{cx}}{B^2} \boldsymbol{\nabla}_\perp \Phi^{(l+1)} \right), \tag{21}$$

where Δ_t is a size of the time step, and $t_l = \Delta_t \cdot l$ corresponds to a discrete time variable. The ion moments in Equation (21) (i.e., $\mathbf{j}_{i,\perp}$ and n_i) are evaluated at the lth time step, and we make use of the $T_e = \text{const}$ assumption [see Section 2].

4 | SIMULATION RESULTS

In this section, we present numerical results from illustrative COGENT simulations performed for parameters characteristic of a DIII-D H-mode. A single ion species deuterium plasma $m_i = 2m_p$ is considered, where m_p is the proton mass. The magnetic geometry and the corresponding grid structure are shown in Figure 1a. The value of the poloidal magnetic field at the intersection of the outer mid-plane and separatrix is given by $B_p \approx 0.4\ T$. To minimize the effects of a short-scale magnetic field noise, which is present in the original EFIT[39] data, both a B-field smoothing technique and the zero-order separation method in Equation (20) are applied. The toroidal magnetic field is given by $RB_\phi = 3.5\ T \cdot m$, and its direction corresponds to the downward ∇B drift. Ion–ion collisions are specified by the fully non-linear Fokker–Planck operator (see Refs. 12, 37, 38 for details), and to describe the radial anomalous transport we adopt the following simple model:

$$T_i^{AN}[B_{\parallel_i}^* f_i] = \boldsymbol{\nabla} \cdot [D(\psi)(\mathbf{e}_\psi \cdot \boldsymbol{\nabla}(B_{\parallel_i}^* f_i))\mathbf{e}_\psi], \tag{22}$$

where $\mathbf{e}_\psi$ is the unit vector in the direction normal to the magnetic flux surfaces. The diffusivity coefficient function is specified by $D(\psi_N) = D_0(0.5 \times \tanh[(0.94 - \psi_N)/0.02] + 0.7)$ in the core and SOL regions, and by $D_{pf}(\psi_N) = D_0(0.5 \times \tanh[(0.95 - x)/0.03)] + 0.7) \times (0.45 \times \tanh[(x - 0.96)/0.02)] + 0.55)$ in the private flux region, where $D_0 = 1.7$ [m^2/s] is the normalization constant, and ψ_N is the normalized flux coordinate (equal to zero at the magnetic axis and unity at the separatrix). The radial diffusion operator in Equation (22) requires two boundary conditions, for which we take $f_i(\psi_{BC}, \theta, v_\parallel, \mu, t) = f_i(\psi_{BC}, \theta, v_\parallel, \mu, t = 0)$, where ψ_{BC} corresponds to the magnetic flux values at the inner core and outer SOL and private flux radial boundaries. In the parallel direction, where only the advection operator is present in Equation (1), we specify an inflow boundary condition to mimic the ion input from recycling $f_i(\psi, \theta_{BC}, v_\parallel{}^{in}, \mu, t) = f_i(\psi, \theta_{BC}, v_\parallel{}^{in}, \mu, t = 0)$, where $v_\parallel{}^{in}$ corresponds to a particle's inflow velocity. The initial condition for the ion distribution is specified by a Maxwellian distribution function with a zero parallel flow velocity and the poloidally uniform density and temperature profiles, given in the core and SOL regions by $n_0(\psi_N) = \overline{n}_0(0.5 \times \tanh[(0.96 - \psi_N)/0.03)] + 0.7)$ and $T_0(\psi_N) = \overline{T}_0(0.3 \times \tanh[(0.96 - \psi_N)/0.03)] + 1.0)$, respectively, where $\overline{n}_0 = 5 \times 10^{19}$ m^{-3} and $\overline{T}_0 = 300$ eV.

The parameters in Equation (16) are specified as follows: The present simplified model (see Section 3) assumes constant $\sigma_\parallel = 8 \times 10^{15}$ s^{-1} and $T_e = 300$ eV. We note that the parameter $\sigma_\parallel$ controls the width of the transition layer, L_E^{sep}, and therefore its value is chosen to be consistent with the near-separatrix value of the electron temperature of 70 eV. On the other hand, the parameter T_e determines the amplitude of poloidal potential variations, and its value is chosen to be the order of the pedestal electron temperature. For the illustrative parameters considered here, poloidal variations of Φ are rather small and therefore the results of simulations should not strongly depend on the value of T_e. In order to mitigate spurious numerical effects, for example, Gibbs oscillations, related to the rapid change in E_r across the separatrix (see Section 2), we take $\nu_{cx}(\psi_N) = \overline{\nu}_{cx} \exp[-(\psi_N - 1.0)^2/\delta_n^2]$, where $\delta_n = 0.01$ and $\overline{\nu}_{cx} = 7.5 \times 10^3$ s^{-1}, which corresponds to an artificially high value of the neutral density, $n_n = 2 \times 10^{16}$ m^{-3}. The initial potential profile corresponds to $e\Phi_0 = -\overline{T}_0 \ln(n_0/\overline{n}_0)$.

Assuming that the radial core boundary lies within a shallow gradient region (e.g., top of a pedestal) we neglect small poloidal variations in the electrostatic potential and adopt the following boundary condition:

$$\left\langle \frac{c^2 n_i m_i}{B^2} |\boldsymbol{\nabla}\psi|^2 \right\rangle \frac{\partial \Phi}{\partial \psi} = \int_0^t dt \langle \boldsymbol{\nabla}\psi \cdot \mathbf{j}_{i,\perp} \rangle. \tag{23}$$

At the SOL and private flux radial boundaries, we take $\partial\Phi/\partial\psi = 0$. Finally, at the divertor plates we arbitrarily set $\Phi = 0$. More accurate radial potential profile near the plates can be determined from the sheath boundary condition,[31,34,35] which requires detailed knowledge of the electron temperature and will be the subject of our future studies. We, however, emphasize again that the present model captures the ion kinetic effects corresponding to ion orbit losses and poloidal variations of the ion distribution

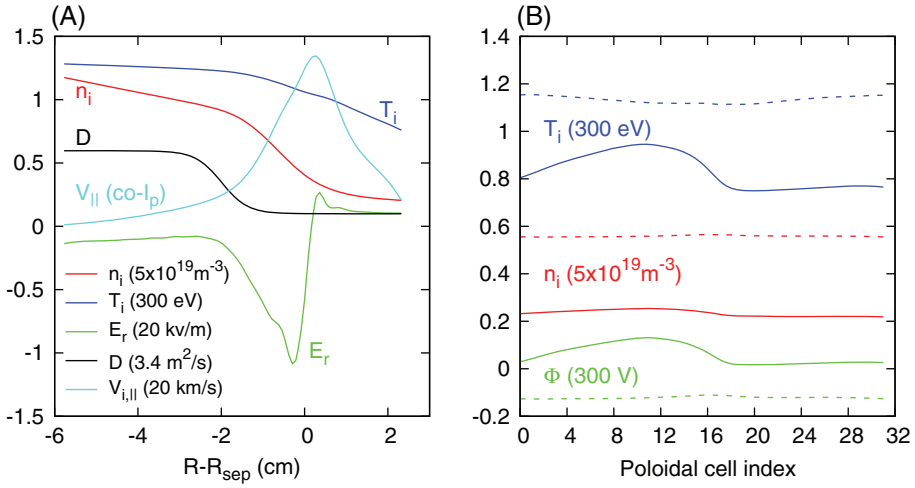

FIGURE 2 (a) Radial profiles of the ion density (n_i), ion temperature (T_i), radial electric field (E_r), anomalous diffusion coefficeint (D), and ion parallel velocity ($V_{i,\|}$) computed along the outboard midplane at $t = 2.8$ ms. The corresponding normalization constants are shown in parentheses. (b) Poloidal profiles of the ion density, temperature, and electrostatic potential obtained on the closed flux surface that intersects the outer midplane 0.4 cm inside the separatrix (dashed curves), and on the open flux surface that intersects the outer mid-plane 0.9 cm outside the separatrix (solid curves). The poloidal index runs in the counter-clockwise direction starting and ending at the core cut on closed field lines, and starting and ending at the low-field-side and high-field-side SOL cuts, respectively, on open field lines (data in the divertor legs is not shown). See Figure 1a for the location of the cuts

function, which play an important role in determining the self-consistent electric fields in the upstream SOL and inside the separatrix.

The results of the numerical simulations are shown in Figures 1–3 and include transport timescale equilibrium solution for 2D plasma profiles (Figure 1) as well as characteristic radial and poloidal lineouts (Figure 2) and a time history for the radial electric field and parallel ion flow (Figure 3a). As expected, a narrow transition layer is observed near the separatrix in the solution for E_r (see Figure 2a). The presence of such structure is inconsistent with the assumptions of the gyrokinetic model in Equation (1) and can affect the near-separatrix results. A detailed analysis of this issue is, however, outside the scope of the present work. Further, we note that the ion temperature in the SOL region is larger at the outer (low-field side) mid-plane than at the inner (high-field side) mid-plane (see Figures 1b and 2b). This observation is qualitatively consistent with the corresponding results of XGC simulations[26]; yet, the temperature variations obtained in the present simulations are less pronounced, plausibly due to the present boundary conditions that force a poloidally uniform temperature distribution at the outer SOL boundary. Poloidal variations of plasma profiles on closed flux surfaces are found to be weak (Figure 2b), consistent with shallow radial temperature gradients (Figure 2a), which determine the deviation of the ion distribution function from a poloidally uniform Maxwellian. Finally, the results for the radial electric field and the co-current parallel ion flow velocity in Figure 2a demonstrate qualitative agreement with the DIII-D experiments.[16,29] Comparing the COGENT model with the analysis performed in Ref. [16], we note that the present simulations include the ion orbit loss and the "Pfirsch–Schluter" mechanisms, both of which can contribute to a co-I_p intrinsic rotation. The turbulence-driven mechanism for edge plasma rotation,[40] which is also used to elucidate the experimental results,[16,40] requires a poloidally varying ballooning structure of the diffusion coefficient D, and therefore is not captured by our model $D = D(\psi)$. However, those effects can be straightforwardly added by extending the transport model in Equation (22) to include poloidally varying D. We also note the other simplifications assumed in the present simulations, such as a uniform electron temperature and the lack of a detailed neutral model, that affect electric fields and plasma flows in the SOL region and will be addressed in our future studies.

The results in Figures 1, 2, and 3a are obtained for the spatial grid resolution specified by ($N_\psi = 22$, $N_\theta = 32$), ($N_\psi = 10$, $N_\theta = 40$), and ($N_\psi = 8$, $N_\theta = 8$), in the core, SOL, and private-flux regions, respectively, and the velocity grid given by ($N_{v_\|} = 36$, $N_\mu = 24$). Here, $N_{\psi,\theta,v_\|,\mu}$ corresponds to the number of cells in the directions of the radial coordinate, poloidal coordinate, parallel velocity, and magnetic moment, respectively. The domain extensions in the velocity space are $-v_\|^{max} < v_\| < v_\|^{max}$ and $0 < \mu < \mu^{max}$, where $v_\|^{\max} = 4\sqrt{2\overline{T}_0/m_i}$, $\mu^{\max} = 4.5\overline{T}_0/B_0$, where $B_0 = 1$ T is the normalization constant. The code performance scales well with the number of processors, and it takes approximately 256 CPU hours (1.33 h × 192 processors) to simulate 1 ms of ion dynamics on the Edison cluster of the NERSC computing system.[41] To address convergence properties of the numerical solutions in Figures 1 and 2, we carried out two additional simulations with twice as many points in either the radial or poloidal directions. The results of these studies are shown in Figure 3b and demonstrate excellent convergence in the poloidal direction. On the other hand, the increase in the radial resolution yields a noticeable change in the numerical solution for E_r within the marginally resolved transition region. Although, the "coarse" and "fine" solutions are close to each other outside the transition region, details of the near-separatrix E_r profile can have a pronounced impact on the intrinsic toroidal rotation and and will be investigated in our future studies.

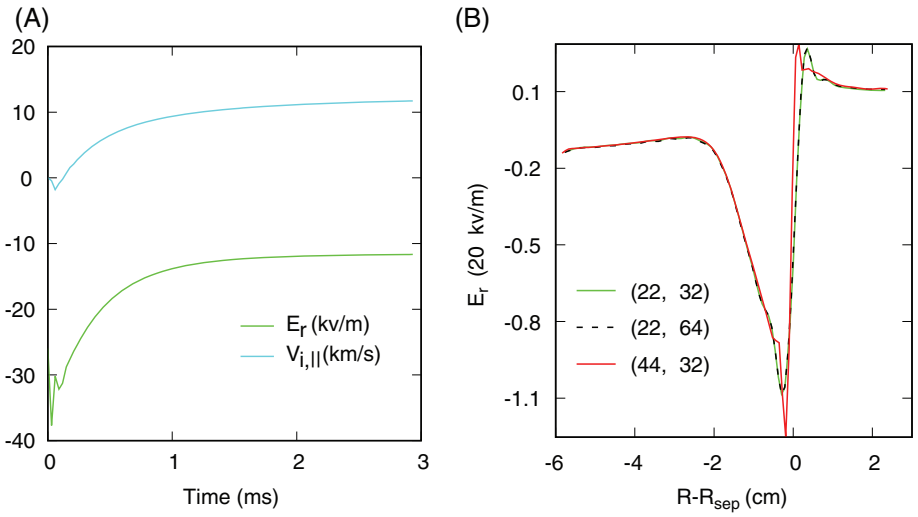

FIGURE 3 (a) Time history of the radial electric field and ion parallel velocity obtained at the outer midplane, 1 cm inside the magnetic separatrix, (b) Radial electric field computed along the outer midplane at $t = 2.8$ ms in the simulations with different spatial grid resolution. The numbers in the parenthesis denote the number of the radial and poloidal cells in the core region, respectively.

5 | CONCLUSION

This paper presents the initial results from continuum drift-kinetic transport simulations that span the magnetic separatrix of a tokamak and include 2D (axisymmetric) self-consistent electrostatic potential variations. The simulations are performed with the COGENT code that employs finite-volume methods combined with the mapped multiblock grid technology. The electrostatic potential variations are determined from the quasi-neutrality equation coupled to an electron fluid model. The simulations also include ion-ion collisions described by the fully-nonlinear Fokker-Plank operator and an anomalous radial transport model. For simplicity, isothermal electrons with $T_e = \text{const}$ are considered and the effects of recycling and neutrals are included via a simple inflow boundary condition for an ion distribution function. The results of illustrative simulations carried out for parameters characteristic of a DIII-D H-mode demonstrate the values of intrinsic rotation and radial electric field qualitatively similar to those observed in DIII-D experiments.[16]

In addition, a near-separatrix transitional structure of the radial electric field is discussed. The influence of neoclassical, anomalous (turbulence), and charge-exchange effects on the width of the transition layer is assessed and a small characteristic length scale, the order of a few ion gyroradii, is concluded. Such a narrow transition structure might be inconsistent with the assumptions of the gyrokinetic model and can also introduce numerical issues. Detailed analysis of these issues along with development of improved models for electrons and neutrals will be a subject of our future studies.

ACKNOWLEDGMENTS

The authors are grateful to R. Cohen, J. Hittinger, T. Rognlien, D. Ghosh, I. Joseph, and M. Umansky for fruitful discussions. They also wish to thank their collaborators in the Applied Numerical Algorithms Group, Lawrence Berkeley National Laboratory (LBNL), for the their assistance in the development of the numerical algorithms and software infrastructure underlying the COGENT code. This research was supported by the U.S. Department of Energy under contract DE-AC52-07NA27344.

REFERENCES

[1] E. A. Belli, J. Candy, *Plasma Phys. Controlled Fusion* **2008**, *50*, 095010.
[2] M. Landreman, F. I. Parra, P. J. Catto, D. R. Ernst, I. Pusztai, *Plasma Phys. Controlled Fusion* **2014**, *56*, 045005.
[3] J. Candy, R. E. Waltz, *J. Comput. Phys.* **2003**, *186*, 545.
[4] F. Jenko, W. Dorland, M. Kotschenreuther, B. N. Rogers, *Phys. Plasmas* **2000**, *7*, 1904.
[5] See https://esl.lbl.gov for edge simulation laboratory (accessed: 23 January, 2018).
[6] M. A. Dorf, R. H. Cohen, M. Dorr, T. Rognlien, J. Hittinger, J. Compton, P. Colella, D. Martin, P. McCorquodale, *Phys. Plasmas* **2013**, *20*, 012513.
[7] M. A. Dorf, M. R. Dorr, J. A. Hittinger, R. H. Cohen, T. D. Rognlien, *Phys. Plasmas* **2016**, *23*, 056102.
[8] M. A. Dorf, R. H. Cohen, M. Dorr, T. Rognlien, J. Hittinger, J. Compton, P. Colella, D. Martin, P. McCorquodale, *Nucl. Fusion* **2013**, *53*, 063015.
[9] P. Colella, M. R. Dorr, J. A. F. Hittinger, D. F. Martin, *J. Comput. Phys.* **2011**, *230*, 2952.
[10] M. Dorr, P. Colella, M. Dorf, D. Ghosh, J. Hittinger, P. Schwartz. *High-order Discretization of a Gyrokinetic Vlasov Model in Edge Plasma Geometry* **2017**.
[11] P. McCorquodale, M. R. Dorr, J. A. F. Hittinger, P. Colella, *J. Comput. Phys.* **2015**, *288*, 181.
[12] M. A. Dorf, R. H. Cohen, M. Dorr, J. Hittinger, T. D. Rognlien, *Contrib. Plasma Phys.* **2014**, *54*, 517.
[13] J. R. Angus, On Anomalous Plasma Transport in The Edge of Magnetic Confinement Devices, Ph.D. Thesis, **2012**.
[14] P. Helander, D. J. Sigma, *Collisional Transport in Magnetized Plasmas*, Cambridge University Press, Cambridge **2002**.
[15] E. Viezzer, T. Pütterich, C. Angioni, A. Bergmann, R. Dux, E. Fable, R. M. McDermott, U. Stroth, E. Wolfrum, the ASDEX Upgrade Team, *Nucl. Fusion* **2014**, *54*, 012003.
[16] J. A. Boedo, J. S. deGrassie, B. Grierson, T. Stoltzfus-Dueck, D. J. Battaglia, D. L. Rudakov, E. A. Belli, R. J. Groebner, E. Hollmann, C. Lasnier, W. M. Solomon, E. A. Unterberg, J. Watkins, *Phys. Plasmas* **2016**, *23*, 092506.

[17] R. M. Churchill, C. Theiler, B. Lipschultz, I. H. Hutchinson, M. L. Reinke, D. Whyte, J. W. Hughes, P. Catto, M. Landreman, D. Ernst, C. S. Chang, R. Hager, A. Hubbard, P. Ennever, J. R. Walk, A. C.-M. Team, *Phys. Plasmas* **2015**, *22*, 056104.
[18] V. Rozhansky, *Plasma Phys. Controlled Fusion* **2004**, *46*, A1.
[19] M. A. Dorf, R. H. Cohen, A. N. Simakov, I. Joseph, *Phys. Plasmas* **2013**, *20*, 082515.
[20] F. I. Parra, P. J. Catto, *Plasma Phys. Controlled Fusion* **2008**, *50*, 065014.
[21] W. W. Lee, *J. Comput. Phys.* **1987**, *72*, 243.
[22] O. V. Batishchev, S. I. Krasheninnikov, P. J. Catto, A. A. Batishcheva, D. J. Sigmar, X. Q. Xu, J. A. Byers, T. D. Rognlien, R. H. Cohen, M. M. Shoucri, I. P. Shkarofskii, *Phys. Plasmas* **1997**, *4*, 1672.
[23] A. V. Chankin, D. P. Coster, N. Asakura, X. Bonnin, G. D. Conway, G. Corrigan, S. K. Erents, W. Fundamenski, J. Horacek, A. Kallenbach, M. Kaufmann, C. Konz, K. Lackner, H. W. Müller, J. Neuhauser, R. A. Pitts, M. Wischmeier, *Nucl. Fusion* **2007**, *47*, 479.
[24] M. Zhao, A. V. Chankin, D. P. Coster, *Nucl. Mater. Energy* **2017**, *12*, 819.
[25] M. A. Dorf, R. H. Cohen, J. C. Compton, M. Dorr, T. D. Rognlien, J. Angus, S. Krasheninnikov, P. Colella, D. Martin, P. McCorquodale, *Contrib. Plasma Phys.* **2012**, *52*, 518.
[26] R. M. Churchill, J. M. Canik, C. S. Chang, R. Hager, A. W. Leonard, R. Maingi, R. Nazikian, D. P. Stotler, *Nucl. Mater. Energy* **2016**, *12*, 978.
[27] G. Dif-Pradalier, P. H. Diamond, V. Grandgirard, Y. Sarazin, J. Abiteboul, X. Garbet, P. Ghendrih, G. Latu, A. Strugarek, S. Ku, C. S. Chang, *Phys. Plasmas* **2011**, *18*, 062309.
[28] T. Vernay, S. Brunner, L. Villard, B. F. McMillan, S. Jolliet, T. M. Tran, A. Bottino, J. P. Graves, *Phys. Plasmas* **2010**, *17*, 122301.
[29] J. S. deGrassie, R. J. Groebner, K. H. Burrell, W. M. Solomon, *Nucl. Fusion* **2009**, *49*, 085020.
[30] S. I. Braginskii, *Rev. Plasma Phys.* **1965**, *1*, 205.
[31] V. A. Rozhansky, S. P. Voskoboynikov, E. G. Kaveeva, D. P. Coster, R. Schneider, *Nucl. Fusion* **2001**, *41*, 387.
[32] R. H. Cohen, M. Dorf, M. Dorr, *Contrib. Plasma Phys.* **2012**, *52*, 529.
[33] V. Rozhansky, E. Kaveeva, S. Voskoboynikov, D. Coster, X. Bonnin, R. Schneider, *Nucl. Fusion* **2003**, *43*, 614.
[34] T. D. Rognlien, D. D. Ryutov, N. Mattor, G. D. Porter, *Phys. Plasmas* **1999**, *6*, 1851.
[35] V. Rozhansky, E. Kaveeva, P. Molchanov, I. Veselova, S. Voskoboynikov, D. Coster, G. Counsell, A. Kirk, S. Lisgo, the ASDEX Upgrade Team, the MAST Team, *Nucl. Fusion* **2009**, *49*, 025007.
[36] I. Joseph, What sets the minimum tokamak scrape-off layer width?, APS Meeting Abstracts, **2016**.
[37] D. Ghosh, M. Dorf, J. Hittinger, M. Dorr, Implicit–explicit time integration for the Vlasov–Fokker–Planck equations, 48th AIAA Plasmadynamics and Lasers Conf, **2016**.
[38] D. Ghosh, M. A. Dorf, M. R. Dorr, J. A. F. Hittinger, *Kinetic Simulation of Collisional Magnetized Plasmas with Semi-Implicit Time Integration, arXiv:1707.08247* 2017.
[39] See https://fusion.gat.com/global/theory/home for efit equilibrium and reconstruction fitting code (accessed: 23 January, 2018).
[40] T. Stoltzfus-Dueck, *Phys. Rev. Lett.* **2012**, *108*, 065002.
[41] See https://nersc.gov for national energy research scientific computing center (accessed: 23 January, 2018).

How to cite this article: Dorf M and Dorr M. Continuum kinetic modelling of cross-separatrix plasma transport in a tokamak edge including self-consistent electric fields, *Contributions to Plasma Physics* 2018;58:434–444. https://doi.org/10.1002/ctpp.201700137.